AIAA SciTech Forum
6-10 January 2020, Orlando, FL
AIAA Scitech 2020 Forum

10.2514/6.2020-1489

Analysis of Interactional Aerodynamics in Multi-Rotor Wind Turbines using Large Eddy Simulations

Ullhas Hebbar*, Jitesh Rane†, Farhan Gandhi‡ and Onkar Sahni§
Center for Mobility with Vertical Lift (MOVE)
Scientific Computation Research Center (SCOREC)
Rensselaer Polytechnic Institute, Troy, NY, 12180

An alternative to traditional upscaling of single-rotor turbines for higher power production is the use of multiple rotors mounted on the same tower. Such multi-rotor configurations have been hypothesized to show improved wake recovery compared to area- and power-equivalent single-rotors with no adverse effect on power production. Analysis of the aerodynamics of multi-rotor configurations using dynamic large eddy simulations (LES) forms the focus of this work, where an actuator line/block model is employed for the rotors to reduce the computational cost. A stochastic turbulence generator is utilized to impose a fluctuating inflow velocity with no associated shear in order to study the effect of incoming turbulence on shear layer breakdown and wake recovery effects. The current results show an early onset of wake recovery in the multi-rotor configuration with a reducing velocity deficit as well as a higher degree of uniformity in the wake compared to the single rotor simulation.

I. Introduction

Potentially severe effects of global climate change have engendered an increasing demand in the modern energy market towards the adoption of renewable sources. For example, the New York State Clean Energy Standard (CES) has set a target of realizing 50% of the state's electricity from renewable sources by 2030, a marked increase from the current share of renewables (under 20%). Under the limitations of current horizontal axis wind turbine technology, such significant increases in power generation capacity are impractical without the use of highly upscaled turbines. Modern 5-6MW turbines have diameters ranging from 120-150m, but diameters are projected to be 200-250m for the 13-20MW turbines, which are of interest to the off-shore wind generation community. At these sizes, classical upscaling models may no longer be cost-effective. Moreover, tooling, manufacturing, transportation and installation costs for these turbines is projected to increase the Levelized Cost of Energy (LCOE), adversely impacting the subsidy-free growth of wind energy in the US.

An alternative to traditional upscaling of single-rotor wind turbines is the use of multi-rotor turbine configurations, where multiple rotors are mounted on the same tower. In multi-rotor turbines, energy capture areas equivalent to large single-rotor turbines can be achieved with blades of smaller span/length, alleviating the high cost associated with manufacturing blades over 100m. Also, long turbine blades experience very large tip deflections and extreme bending loads necessitating expensive on-blade load-mitigating technology, which can be avoided by adopting multi-rotor configurations. Despite the several advantages presented by multi-rotor turbines, the aerodynamic behavior of the multi-rotor turbine including power production and wake recovery remains a topic of interest in the wind energy community.

Vestas Wind Energy Systems A/S is the first major corporate entity to have built a modern utility-scale multi-rotor wind turbine in collaboration with DTU, Denmark, as a demonstrator. Four V29-225KW rotors were mounted on a 74m high tower in the DTU campus, resulting in a 900KW turbine [1]. Their recently published results suggest an up to 2% gain in power due to rotor interaction at lower wind speeds. Further, the multi-rotor (MR) configuration showed faster wake recovery compared to an equivalent single-rotor (SR) turbine with the same total swept area, power and thrust values. An important distinction to note between the SR and MR configurations is the close proximity of the rotors in the MR turbine which results in strong aerodynamic interaction. *Chasapogiannis et al.* [2] used vortex-based

*PhD Student, Department of Mechanical, Aerospace, and Nuclear Engineering, RPI
†PhD Student, Department of Mechanical, Aerospace, and Nuclear Engineering, RPI, and AIAA Student Member
‡Professor and Rosalind and John J. Redfern Jr. '33 Endowed Chair in Aerospace Engineering, Department of Mechanical, Aerospace and Nuclear Engineering, RPI, and AIAA Associate Fellow
§Associate Professor, Department of Mechanical, Aerospace, and Nuclear Engineering, RPI, and AIAA Senior Member

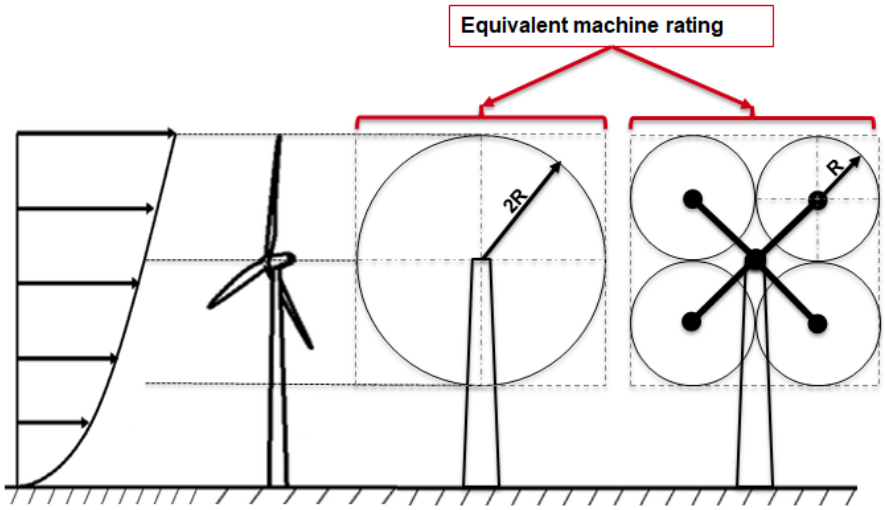

Fig. 1 Schematic of a quad-rotor configuration with the equivalent single-rotor turbine

and CFD models to analyze seven 2MW single rotors, reporting an increase in power and thrust compared to seven non-interacting rotors. They also observed a merging of the individual wakes into a single structure about two rotor diameters downstream. In a large scale energy generation study, *Jamieson et al.* [3] analyzed a multi-rotor turbine rated at 20MW consisting of forty-five 444kW rotors. An increased performance in power production was reported; this was claimed to be due to increased rotor-rotor interaction and a faster response to wind speed variations. More recently, *Ghasias et al.* [4] used LES to demonstrate a faster wake recovery and lower wake turbulent kinetic energy for a MR turbine as compared to an equivalent SR turbine. It was hypothesized that a larger entrainment led to these effects, as the rotor perimeter to swept area ratio for a MR turbine is twice that of a SR turbine. However, these studies used relatively coarse grids (i.e., up to 40 grid points over rotor diameter), which is not sufficient to accurately resolve the near wake flow structures.

The present work is focused on the study of near wake dynamics in a MR turbine configuration similar to the Vestas concept as shown in Figure 1. The MR configuration is compared with an equivalent SR turbine with twice the diameter of the individual rotors in the MR (i.e., the total swept area is the same). The current study employs LES, which makes the problem computationally tractable as compared to direct numerical simulation (DNS), while maintaining sufficient accuracy with about 120 grid points across the rotor diameter. It is commonly known that ambient atmospheric turbulence leads to faster shear layer breakdown in the wind turbine wake as well as faster wake recovery [5]. In this study, a stochastic turbulence generator is used to impose a turbulent inflow upstream of the turbine. Axial velocity deficit as well as added wake turbulent intensity due to the turbine is examined and wake recovery is compared between the MR and equivalent SR configurations.

This paper is organized as follows. The dynamic LES formulation is discussed in Section II, while the actuator line method and turbine models are briefly discussed in Section III.A and Section III.B, respectively . Details of the turbulent inflow implementation are provided in Section IV. Results of the study are presented in Section V, and finally a brief conclusion and description of the future work in Section VI rounds up the paper.

II. Dynamic Large Eddy Simulation

A. Combined Model Formulation

This work uses the incompressible Navier Stokes equations in the arbitrary Lagrangian Eulerian (ALE) description. The strong form of the equations is given as

$$
\begin{aligned}
&u_{k,k} = 0 \\
&u_{i,t} + (u_j - u_j^m)u_{i,j} = -p_{,i} + \tau_{ij,j}^{\nu} + f_i
\end{aligned}
\tag{1}
$$

where u_i is the velocity vector, u_i^m is the mesh velocity vector, p is the pressure (scaled by the constant density), $\tau_{ij}^{\nu} = 2\nu S_{ij}$ is the symmetric (Newtonian) viscous stress tensor (scaled by the density), ν is the kinematic viscosity, $S_{ij} = 0.5(u_{i,j} + u_{j,i})$ is the strain-rate tensor, and f_i is the body force vector (per unit mass). Note that Einstein summation notation is used.

The weak form is stated as follows: find $\mathbf{u} \in \boldsymbol{\mathcal{S}}$ and $p \in \mathcal{P}$ such that

$$
\begin{aligned}
B(\{w_i, q\}, \{u_i, p\}; u_l^m) = &\int_{\Omega} [w_i(u_{i,t} + u_i u_{j,j}^m) + w_{i,j}(-u_i(u_j - u_j^m) + \tau_{ij}^{\nu} - p\delta_{ij}) - q_{,k}u_k]\, d\Omega \\
&+ \int_{\Gamma_h} [w_i(u_i(u_j - u_j^m) - \tau_{ij}^{\nu} + p\delta_{ij})n_j + qu_k n_k]\, d\Gamma_h \\
&= \int_{\Omega} w_i f_i d\Omega
\end{aligned}
\tag{2}
$$

for all $\mathbf{w} \in \boldsymbol{\mathcal{W}}$ and $q \in \mathcal{P}$. $\boldsymbol{\mathcal{S}}$ and $\mathcal{P}$ are suitable trial/solution spaces and $\boldsymbol{\mathcal{W}}$ is the test/weight space. $\mathbf{w}$ and q are the weight functions for the velocity and pressure variables, respectively. Ω is the spatial domain and Γ_h is the portion of the domain boundary with Neumann or natural boundary conditions.

The above weak form can be written concisely as: find $\boldsymbol{U} \in \boldsymbol{\mathcal{U}}$ such that

$$
B(\boldsymbol{W}, \boldsymbol{U}; u_l^m) = (\boldsymbol{W}, \boldsymbol{F}) \tag{3}
$$

for all $\boldsymbol{W} = [\mathbf{w}, q]^T \in \boldsymbol{\mathcal{V}}$. $\boldsymbol{U} = [\mathbf{u}, p]^T$ is the vector of unknown solution variables and $\boldsymbol{F} = [\mathbf{f}, 0]^T$ is the source vector. The solution and weight spaces are: $\boldsymbol{\mathcal{U}} = \{\boldsymbol{U} = [\mathbf{u}, q]^T | \mathbf{u} \in \boldsymbol{\mathcal{S}}; p \in \mathcal{P}\}$ and $\boldsymbol{\mathcal{V}} = \{\boldsymbol{W} = [\mathbf{w}, q]^T | \mathbf{w} \in \boldsymbol{\mathcal{W}}; q \in \mathcal{P}\}$, respectively.

Throughout this text $B(\cdot, \cdot)$ is used to represent the semi-linear form that is linear in its first argument and $(\cdot, \cdot)$ is used to denote the L_2 inner product. $B(\boldsymbol{W}, \boldsymbol{U}; u_l^m)$ is split into bilinear and semi-linear terms as shown below.

$$
B(\boldsymbol{W}, \boldsymbol{U}; u_l^m) = B_1(\boldsymbol{W}, \boldsymbol{U}; u_l^m) + B_2(\boldsymbol{W}, \boldsymbol{U}) = (\boldsymbol{W}, \boldsymbol{F}) \tag{4}
$$

where $B_1(\boldsymbol{W}, \boldsymbol{U}; u_l^m)$ contains the bilinear terms and $B_2(\boldsymbol{W}, \boldsymbol{U})$ consists of the semi-linear terms. These are defined as

$$
\begin{aligned}
B_1(\boldsymbol{W}, \boldsymbol{U}; u_l^m) = &\int_{\Omega} [w_i(u_{i,t} + u_i u_{j,j}^m) + w_{i,j}(u_i u_j^m + \tau_{ij}^{\nu} - p\delta_{ij}) - q_{,k}u_k]\, d\Omega \\
&+ \int_{\Gamma_h} [w_i(-u_i u_j^m - \tau_{ij}^{\nu} + p\delta_{ij})n_j + qu_k n_k]\, d\Gamma_h
\end{aligned}
\tag{5}
$$

$$
B_2(\boldsymbol{W}, \boldsymbol{U}) = -\int_{\Omega} w_{i,j} u_i u_j d\Omega + \int_{\Gamma_h} w_i u_i u_j n_j d\Gamma_h \tag{6}
$$

The Galerkin weak form is obtained by considering the finite-dimensional or discrete solution spaces $\boldsymbol{\mathcal{S}}^h \subset \boldsymbol{\mathcal{S}}$ and $\mathcal{P}^h \subset \mathcal{P}$ and the weight space $\boldsymbol{\mathcal{W}}^h \subset \boldsymbol{\mathcal{W}}$, where the superscript h is used as a mesh parameter to denote discretized spaces and variables in a finite element context. Using these spaces, $\boldsymbol{\mathcal{U}}^h = \{\boldsymbol{U}^h = [\mathbf{u}^h, p^h]^T | \mathbf{u}^h \in \boldsymbol{\mathcal{S}}^h; p^h \in \mathcal{P}^h\}$ and $\boldsymbol{\mathcal{V}}^h = \{\boldsymbol{W}^h = [\mathbf{w}^h, q^h]^T | \mathbf{w}^h \in \boldsymbol{\mathcal{W}}^h; q^h \in \mathcal{P}^h\}$ are defined. The Galerkin weak form is then stated concisely as: find $\boldsymbol{U}^h \in \boldsymbol{\mathcal{U}}^h$ such that

$$
B(\boldsymbol{W}^h, \boldsymbol{U}^h) = (\boldsymbol{W}^h, \boldsymbol{F}) \tag{7}
$$

for all $\boldsymbol{W}^h \in \mathcal{V}^h$. Note for brevity we have dropped u_l^m term in the arguments of the semi-linear form. The Galerkin weak formulation corresponds to a method for direct numerical simulation since no modeling is employed. However, when the finite-dimensional spaces are incapable of representing the fine/small scales, the Galerkin formulation yields an inaccurate solution. A model term is added to overcome this difficulty, e.g., as done in the residual-based variational multiscale (RBVMS) formulation.

In RBVMS, a set of model terms is added to the Galerkin weak form that results in the following variational formulation: find $\boldsymbol{U}^h \in \mathcal{U}^h$ such that

$$B(\boldsymbol{W}^h, \boldsymbol{U}^h) + M_{rbvms}(\boldsymbol{W}^h, \boldsymbol{U}^h) = (\boldsymbol{W}^h, \boldsymbol{F}) \tag{8}$$

for all $\boldsymbol{W}^h \in \mathcal{V}^h$. M_{rbvms} represents the set of model terms due to the RBVMS approach.

A scale separation is used to decompose the solution and weight spaces as $\mathcal{S} = \mathcal{S}^h \oplus \mathcal{S}'$ and $\mathcal{P} = \mathcal{P}^h \oplus \mathcal{P}'$, and $\mathcal{W} = \mathcal{W}^h \oplus \mathcal{W}'$, respectively. Thus, the solution and weight functions are decomposed as $u_i = u_i^h + u_i'$ and $p = p^h + p'$ or $\boldsymbol{U} = \boldsymbol{U}^h + \boldsymbol{U}'$, and $w_i = w_i^h + w_i'$ and $q = q^h + q'$ or $\boldsymbol{W} = \boldsymbol{W}^h + \boldsymbol{W}'$, respectively. Note that coarse-scale or resolved quantities are denoted by $(\cdot)^h$ and fine-scale or unresolved quantities by $(\cdot)'$. The coarse-scale quantities are resolved by the grid whereas the effects of the fine scales on the coarse scales are modeled. In RBVMS, the fine scales are modeled as a function of the strong-form residual due to the coarse-scale solution. This is represented abstractly as $\boldsymbol{U}' = \mathcal{F}(\boldsymbol{R}(\boldsymbol{U}^h); \boldsymbol{U}^h)$, where $\boldsymbol{R}(\cdot) = [\boldsymbol{R}^m(\cdot), R^c(\cdot)]^T$ is the strong-form residual of the equations with $\boldsymbol{R}^m(\cdot)$ (or $R_i^m(\cdot)$) and $R^c(\cdot)$ as those of the momentum and continuity equations, respectively. Specifically, the fine-scale quantities are modeled as $u_i' \approx -\tau_M R_i^m(u_k^h, p^h; u_l^m)$ and $p' \approx -\tau_C R^c(u_k^h)$, where τ_C and τ_M are stabilization parameters (e.g., see details in Tran and Sahni [6]). This provides a closure to the coarse-scale problem as it involves coarse-scale solution as the only unknown. This is why $M_{rbvms}(\boldsymbol{W}^h, \boldsymbol{U}^h)$ is written only in terms of the unknown coarse-scale solution $\boldsymbol{U}^h$. In summary, $M_{rbvms}(\boldsymbol{W}^h, \boldsymbol{U}^h)$ can be written as

$$\begin{aligned}
&M_{rbvms}(\boldsymbol{W}^h, \boldsymbol{U}^h) = \\
&\sum_e \int_{\Omega_e^h} [\underbrace{-(w_i^h u_{j,j}^m + w_{i,j}^h u_j^m)\tau_M R_i^m(u_k^h, p^h; u_l^m)}_{M_{rbvms}^{ALE}(\boldsymbol{W}^h, \boldsymbol{U}^h)} \\
&\quad + \underbrace{q_{,i}^h \tau_M R_i^m(u_k^h, p^h; u_l^m)}_{M_{rbvms}^{cont}(\boldsymbol{W}^h, \boldsymbol{U}^h)} + \underbrace{w_{i,j}^h \tau_C R^c(u_k^h)\delta_{ij}}_{M_{rbvms}^{P}(\boldsymbol{W}^h, \boldsymbol{U}^h)} \\
&\quad + \underbrace{w_{i,j}^h \left(u_i^h \tau_M R_j^m(u_k^h, p^h; u_l^m) + \tau_M R_i^m(u_k^h, p^h; u_l^m) u_j^h\right)}_{M_{rbvms}^{C}(\boldsymbol{W}^h, \boldsymbol{U}^h)} \\
&\quad \underbrace{-w_{i,j}^h \tau_M R_i^m(u_k^h, p^h; u_l^m)\tau_M R_j^m(u_k^h, p^h)}_{M_{rbvms}^{R}(\boldsymbol{W}^h, \boldsymbol{U}^h)}] d\Omega_e^h
\end{aligned} \tag{9}$$

Note that all model terms are written in terms of the resolved scales within each element (where e denotes an element and contributions from all elements are summed). The last model term is used to represent the Reynolds stresses (i.e., M_{rbvms}^R) while the two terms prior to it are used to represent the cross-stress terms (i.e., M_{rbvms}^C).

In previous studies [7, 8], it was found that the RBVMS model provides a good approximation for the turbulent dissipation due to the cross stresses but the dissipation due to the Reynolds stresses is underpredicted and turns out to be insufficient. Therefore, a combined subgrid-scale model was employed which uses the RBVMS model for the cross-stress terms and the dynamic Smagorinsky eddy-viscosity model for the Reynolds stress terms. This was done in both a finite element code [8, 9] and a spectral code [7]. The combined subgrid-scale model is defined as

$$B(\boldsymbol{W}^h, \boldsymbol{U}^h) + M_{comb}(\boldsymbol{W}^h, \boldsymbol{U}^h; C_S, h) = (\boldsymbol{W}^h, \boldsymbol{F}) \tag{10}$$

where

$$
\begin{aligned}
M_{comb}(\boldsymbol{W}^h, \boldsymbol{U}^h; C_S, h) =& M^{ALE}_{rbvms}(\boldsymbol{W}^h, \boldsymbol{U}^h) + M^{cont}_{rbvms}(\boldsymbol{W}^h, \boldsymbol{U}^h) \\
&+ M^{P}_{rbvms}(\boldsymbol{W}^h, \boldsymbol{U}^h) + M^{C}_{rbvms}(\boldsymbol{W}^h, \boldsymbol{U}^h) \\
&+ (1-\gamma) M^{R}_{rbvms}(\boldsymbol{W}^h, \boldsymbol{U}^h) \\
&+ \gamma M^{R}_{smag}(\boldsymbol{W}^h, \boldsymbol{U}^h; C_S, h)
\end{aligned} \tag{11}
$$

$$
M^{R}_{smag}(\boldsymbol{W}^h, \boldsymbol{U}^h; C_S, h) = \int_{\Omega} w^h_{i,j} 2 \underbrace{(C_S h)^2 |S^h|}_{\nu_t} S^h_{ij} d\Omega \tag{12}
$$

where ν_t is the eddy viscosity, $|S^h|$ is the norm of the strain-rate tensor (i.e., $|S^h| = \sqrt{2\boldsymbol{S}^h : \boldsymbol{S}^h} = \sqrt{2 S^h_{ij} S^h_{ij}}$), h is the local mesh size, and C_S is the Smagorinsky parameter. The parameter γ is set to be either 0 or 1 in order to control which model is used for the Reynolds stresses. Note that $\gamma = 0$ results in the original RBVMS model and $\gamma = 1$ results in the combined subgrid-scale model. In this study, $\gamma = 1$ is employed. The Smagorinsky parameter is computed dynamically in a local fashion as discussed below.

B. Dynamic Procedure

To dynamically compute the Smagorinsky parameter in a local fashion, we follow the localized version of the variational Germano identity (VGI) developed by Tran *et al.* [6]. In this procedure, Lagrangian averaging along fluid pathtubes is applied to make it robust and which maintains the localized nature of the VGI. The dynamic local procedure and the associated approximations are summarized in this section.

1. Local Variational Germano Identity

The VGI involves comparing the variational form (including the model terms) between different levels of the discretization such that they are nested. In the localized version of the VGI, a set of nested spaces are constructed by using a series of coarser second-level grids along with the primary or original grid. We refer to the primary grid as the h-grid and any grid in the series of second-level grids as the H-level grid. Each H-level grid is chosen such that it is associated with an interior node in the primary grid. This is done such that each H-grid is identical to the h-grid except that the given node k in the h-grid is coarsened or removed resulting in a nested H-level grid for node k, which we refer to as the H_k-grid. Note that each H_k-grid involves local coarsening around a given node k while the remainder of the mesh remains the same. This is demonstrated in 1-D in Figure 2, where Ω^{H_k} is the macro element in the H_k-grid corresponding to node k while Ω^{P_k} is the corresponding patch of elements around node k in the h-grid. Note that $k = 1, 2, \ldots, n_{intr}$, where n_{intr} is the number of interior nodes in the h-grid. Therefore, there are n_{intr} grids at the H level, each of which is paired with the primary h-grid. This results in the following spaces for each interior node, $\boldsymbol{\mathcal{U}}^{H_k} \subset \boldsymbol{\mathcal{U}}^h \subset \boldsymbol{\mathcal{U}}$ and $\boldsymbol{\mathcal{V}}^{H_k} \subset \boldsymbol{\mathcal{V}}^h \subset \boldsymbol{\mathcal{V}}$, for the solution and weight functions, respectively.

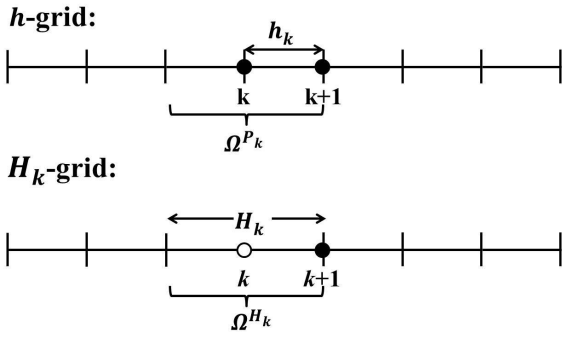

Fig. 2 1-D schematic of the h- and H-level grids for local VGI

The local VGI procedure then uses the H_k-grids with the h-grid to compute the model parameter at every node k in the h-grid. By setting $\boldsymbol{W}^h = \boldsymbol{W}^{H_k}$, since $\boldsymbol{\mathcal{V}}^{H_k} \subset \boldsymbol{\mathcal{V}}^h \subset \boldsymbol{\mathcal{V}}$, we get (for details see Ref. [6]).

$$M_{comb}(\boldsymbol{W}^{H_k}, \boldsymbol{U}^h; C_S^k, h_k) - M_{comb}(\boldsymbol{W}^{H_k}, \boldsymbol{U}^{H_k}; C_S^k, H_k) = -(B(\boldsymbol{W}^{H_k}, \boldsymbol{U}^h) - B(\boldsymbol{W}^{H_k}, \boldsymbol{U}^{H_k})) \tag{13}$$

We recognize that determining $\boldsymbol{U}^{H_k}$ for each interior node k involves a grid-level computation or projection (operations which involve looping over the elements of the H_k-grid). This is prohibitive and therefore, a surrogate is considered. $\boldsymbol{U}^{H_k}$ is approximated within the macro element using a volume-weighted average of $\boldsymbol{U}^h$ while outside of the macro element the solution is assumed to be the same between the two grid levels. This assumption further bypasses a grid-level computation. This assumption arises from the requirement on the variational multiscale (VMS) method to provide a localization at the element level and the desire to yield nodal exactness at element corners [10]. This leads to $\boldsymbol{U}^{H_k} \approx \widetilde{\boldsymbol{U}}^{H_k}|_{\Omega^{H_k}} = \mathbb{A}^{H_k}(\boldsymbol{U}^h)$, where $\mathbb{A}^{H_k}$ is the local averaging operator defined below.

$$\mathbb{A}^{H_k}(f^h) = \frac{1}{|\Omega^{P_k}|} \int\limits_{\Omega_e^h \in \Omega^{P_k}} f^h d\Omega_e^h \tag{14}$$

where $|\Omega^{P_k}|$ is the volume of the local patch and Ω_e^h indicates an element in the h-grid.

This choice is only feasible when the spatial derivatives exist on the weight function. In addition, instead of using $\widetilde{\boldsymbol{U}}^{H_k}$ to compute $\boldsymbol{S}^{H_k}$, $\boldsymbol{S}^{H_k}$ is also approximated within the macro element as $\widetilde{\boldsymbol{S}}^{H_k}|_{\Omega^{H_k}} \approx \mathbb{A}^{H_k}(\boldsymbol{S}^h)$. Furthermore, among all of the terms in Equation (13) not involving the unknown model parameter, the non-linear convective term is found to be dominating [6]. We note that this assumption holds exactly in a spectral setting where all the bilinear terms cancel out between the H- and h-level grids due to the L_2 orthogonality of spectral modes [11]. The local VGI simplifies to

$$M_{smag}(\boldsymbol{W}^{H_k}, \boldsymbol{U}^h; C_S^k, h_k)_{\Omega^{P_k}} - M_{smag}(\boldsymbol{W}^{H_k}, \widetilde{\boldsymbol{U}}^{H_k}; C_S^k, H_k)_{\Omega^{H_k}} = - (B_2(\boldsymbol{W}^{H_k}, \boldsymbol{U}^h)_{\Omega^{P_k}} - B_2(\boldsymbol{W}^{H_k}, \widetilde{\boldsymbol{U}}^{H_k})_{\Omega^{H_k}}) \tag{15}$$

Now an appropriate choice for $\boldsymbol{W}^{H_k} \in \boldsymbol{\mathcal{V}}^{H_k}$ must be made. In a 1D setting, we select $\boldsymbol{W}^{H_k} = [w_i^{H_k}, 0]^T$ with $w_i^{H_k}$ such that it is linear along a spatial direction within the macro element and is constant or flat outside. Within the macro element, $w_i^{H_k}$ is selected such that

$$w_{i,j}^{H_k} = \frac{1}{|\Omega^{H_k}|} \tag{16}$$

where $|\Omega^{H_k}|$ is the volume of the element. This choice of $\boldsymbol{W}^{H_k}$ is feasible in a multi-D setting and on an unstructured mesh consisting elements of mixed topology, however, a larger patch must be considered. An extra layer of elements is needed around the macro element to attain a constant value in the outside region. This extra layer acts as a buffer region. This choice is made due to its ease of implementation. For more details see Ref. [6].

2. Local VGI Computation

At this point we drop the subscript k in H_k and P_k and superscript k in C_S^k for brevity and only use it when necessary. The residual of the local VGI is defined as

$$\epsilon_{ij} = L_{ij} - 2(C_S h)^2 M_{ij} \tag{17}$$

where

$$L_{ij} = \left(\left(\frac{1}{|\Omega^H|}, u_i^h u_j^h\right)_{\Omega^P} - \left(\frac{1}{|\Omega^H|}, \widetilde{u}_i^H \widetilde{u}_j^H\right)_{\Omega^H}\right) \tag{18}$$

$$M_{ij} = \left(\left(\frac{1}{|\Omega^H|}, |S^h| S_{ij}^h\right)_{\Omega^P} - \left(\frac{H}{h}\right)^2 \left(\frac{1}{|\Omega^H|}, |\widetilde{S}^H| \widetilde{S}_{ij}^H\right)_{\Omega^H}\right) \tag{19}$$

The least squares method is applied to determine the model parameter as follows

$$(C_S h)^2 = \frac{1}{2} \frac{L_{ij} M_{ij}}{M_{ij} M_{ij}} \tag{20}$$

Since the local VGI procedure often leads to negative values for $(C_S h)^2$, an averaging scheme is employed to avoid this issue. Specifically, Lagrangian averaging is applied [12]. To do so, two additional advection-relaxation scalar equations are solved. These are shown in Equations (21) and (22). The scalars I_{LM} and I_{MM} in these equations are the Lagrangian-averaged counterparts of $L_{ij}M_{ij}$ and $M_{ij}M_{ij}$, respectively.

$$I_{LM,t} + (u_j - u_j^m)I_{LM,j} = \frac{1}{T}(L_{ij}M_{ij} - I_{LM}) \tag{21}$$

$$I_{MM,t} + (u_j - u_j^m)I_{MM,j} = \frac{1}{T}(M_{ij}M_{ij} - I_{MM}) \tag{22}$$

where T is the timescale over which averaging is applied. Additionally, a local volume-weighted averaging is also applied separately to the numerator and denominator of Equation (20) as follows

$$(C_S h)^2 = \frac{1}{2}\frac{\mathbb{A}^H(I_{LM})}{\mathbb{A}^H(I_{MM})} \tag{23}$$

where, as before, $\mathbb{A}^H$ represents a local averaging operator. This is equivalent to averaging over local pathtubes [6, 9] and maintains the utility of the local VGI.

III. Actuator Line and Turbine Models

A. Actuator Line Method

In order to reduce the computational overhead involved in fully resolving the airfoil geometry as well as the associated boundary layers for wind turbine blades, Blade Element Momentum Theory (BEMT) [13] is employed as a reduced order model for the rotor in this work. In BEMT, the sectional lift and drag forces on the rotor are assumed to vary only along the radial direction (r), i.e., along the span. BEMT computations use local lift and drag coefficients (C_l, C_d) from airfoil tables in conjunction with the local relative velocity (V_{rel}) and chord (c) length at a given radial location to find the lift and drag per unit span

$$(L, D) = \frac{1}{2}(C_l, C_d)\rho V_{rel}^2 c \tag{24}$$

In the Actuator Line Model (ALM) [14], force values are applied as volumetric source terms in the Navier-Stokes equations within a fictitious region around actuator lines, which model the blades of the turbine. This width of this fictitious region is typically chosen to be on the order of c. In order to prevent numerical instability, the force per unit span (i.e., function of r) is distributed over the fictitious region using a fixed half-width, γ, in both the azimuthal (θ) and axial (z) directions. The force term is integrated numerically over finite elements that reside within this fictitious region at any given instance of time. The force (per unit volume) in CFD is defined as

$$\mathbf{f_{3D}}^{CFD} = \mathbf{f_{1D}}^{BEM}(r)\delta(z)\delta(\theta) \tag{25}$$

where the following cubic spline distribution kernel (for $|z| \leq \gamma$) with unit area is used (similar kernel is used in the azimuthal direction)

$$\begin{cases} t_0 = \frac{z+\gamma}{\gamma}; \quad \delta(z) = \frac{1}{\gamma}\left[-2t_0^3 + 3t_0^2\right] & ; \quad z < 0 \\ t_0 = \frac{z}{\gamma}; \quad \delta(z) = \frac{1}{\gamma}\left[2t_0^3 - 3t_0^2 + 1\right] & ; \quad z \geq 0 \end{cases} \tag{26}$$

B. Turbine Model

In this study, a MR turbine with four equal rotors is considered along with an equivalent SR turbine. The MR turbine consists of four counter-rotating 1.5MW rotors with a tip clearance of 2.5% diameter of the SR turbine. The freely available NREL WindPACT 1.5MW rotor [15] is used for each rotor of the MR configuration while a linearly scaled (to 6MW) model of the NREL 5MW reference turbine [16] is used as the equivalent SR turbine to compare against the MR turbine. The operating parameters of the turbines are given in Table 1 where D/c_r is the ratio of the diameter to the

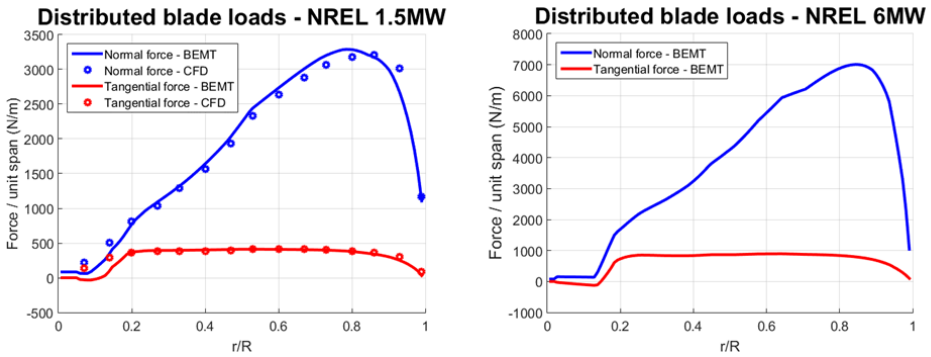

Fig. 3 Distributed loads from BEMT for the NREL 1.5MW and NREL 6MW turbines

Table 1 Operating parameters of turbines

Parameters	NREL 1.5MW	NREL 6MW
Diameter (D)	70m	140m
D/c_r ratio	25.52	27.08
Rated wind speed	11.4 m/s	11.4m/s
Rated RPM	21.8	10.9
Collective pitch	3.2°	0.8°

root chord of the blade. This c_r will be used in the subsequent sections to specify the mesh size used in the current simulations.

As mentioned earlier, the ALM implementation requires sectional blade load values to be applied as source terms in the Navier Stokes equations. Figure 3 shows the normal and tangential forces computed using BEMT for the NREL 1.5MW and NREL 6MW turbines as a function of the non-dimensional radial coordinate (r). As a reference, the BEMT loads computed for the NREL 1.5MW turbine are compared with blade-resolved CFD results obtained by *Kirby et al.* [17], showing a close agreement.

The BEMT results for both turbines show nearly constant tangential force (F_t) over the span of the blade except near the root and tip (due to loss correction in BEMT). F_t is directly related to the power generated by the rotors, and the SR and MR turbines produce identical power (6 MW) after accounting for a 95% generator efficiency.

The thrust (or normal force F_n) produced by the rotors generally increases from the inboard to the outboard section, and this F_n is primarily responsible for the axial velocity deficit behind the rotor. It is to be noted in general that the thrust is higher than F_t by a factor of about 4-5. Although the power production remains the same between the SR and MR turbines, this is not true of the net thrust produced since the blades of the two turbines are composed of different airfoils. The SR turbine produces 815 kN of thrust while the MR turbine produces 858 kN of thrust which is roughly 5% higher than that of the SR turbine. However, the effect of this difference on the axial velocity deficit in the wake is expected to be minor as the thrust scales with the square of V_z.

IV. Turbulent Inflow

There are several methods to generate incoming turbulent wind data (with or without shear), for example, the precursor simulation method and the resolved upstream turbulence method. The former involves simulating a fully turbulent atmospheric flow over a relatively coarse grid, and using two-dimensional/planar profiles of velocity from a suitable location as an inlet boundary condition for the more expensive wind turbine simulation [18]. The latter involves using a stochastic turbulent wind-field generator such as TurbSim [19], which is used in this study. TurbSim, developed by NREL provides turbulent flowfields of neutrally stable atmospheric boundary layers. Although several models for the velocity spectra are available, the Kaimal spectrum was utilized as per the IEC 61400-3 standard.

This study is restricted to turbulent inflow with no shear since the current focus is on comparing aerodynamics (e.g., shear layer breakdown and wake recovery) between SR and MR turbines under turbulent conditions. Turbulent inflow with shear will be considered in a future study.

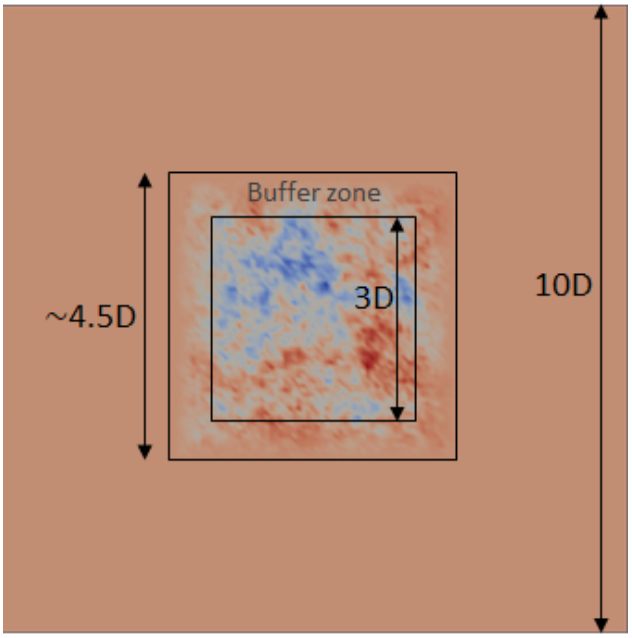

Fig. 4 View of inlet with turbulent patch and buffer zone

A turbulent flow-field with a mean axial velocity (V_∞) of 11.4 m/s (equal to the rated wind speed of both turbines) and an incoming turbulent intensity ($TI = V_z^{RMS}/V_\infty$) of 0.075 is obtained from TurbSim, where V_z^{RMS} is the root mean square computed for the axial velocity. This value of TI is close to the one used by Churchfield *et al.* [20] for their neutral stability simulations as well as the TI measured in mid-western low to moderate roughness conditions [21]. A time step of 0.1s and a spatial resolution of $2c_r$ corresponding to the single rotor is used for the simulation over a period of 450s.

Instead of imposing resolved turbulence over the entire inlet, a $3D \times 3D$ turbulent 'patch' defined over part of the inlet is deemed sufficient to prevent the surrounding non-turbulent flowfield from influencing the turbine wake. The turbulent inflow is imposed $4D$ upstream of the turbine over an area of $4.5D \times 4.5D$, where $3D \times 3D$ turbulent patch resides in the center and a buffer zone of size roughly $0.75D$ (with 10 grid points) is used on each side to smoothly transition from the turbulent flow to the uniform free-stream (at V_∞). It should be noted that the 'D' used here and henceforth denotes the rotor diameter of the SR turbine..

V. Results and Discussion

A. Problem Setup and Discretization

The SR 6MW and the MR 4×1.5MW turbine simulations use a similar problem setup and discretization. Air properties used for the simulation are a density of $\rho = 1.225$ kg/m^3 and a kinematic viscosity of $\nu = 1.5 \times 10^{-5}$ m^2/s. In order to distribute the blade loads for the ALM implementation, a half-width of $\gamma = c_r$ is used, which is different for the SR and MR turbines.

The computational domain under consideration is of size $10D \times 10D \times 20D$ with the largest dimension in the stream-wise/axial (z) direction. A global size of $4c_r$ is specified for the mesh. Several refinement zones are added for the SR and MR turbine simulations. A sectional view of the mesh for the SR simulation is presented in Figure 5 where the mesh size in the box refinement zone R4 is $2c_r$ corresponding to the root chord in the SR turbine. This is the mesh resolution on which turbulent inflow is applied at the inlet patch and propagated downstream. A cylindrical refinement

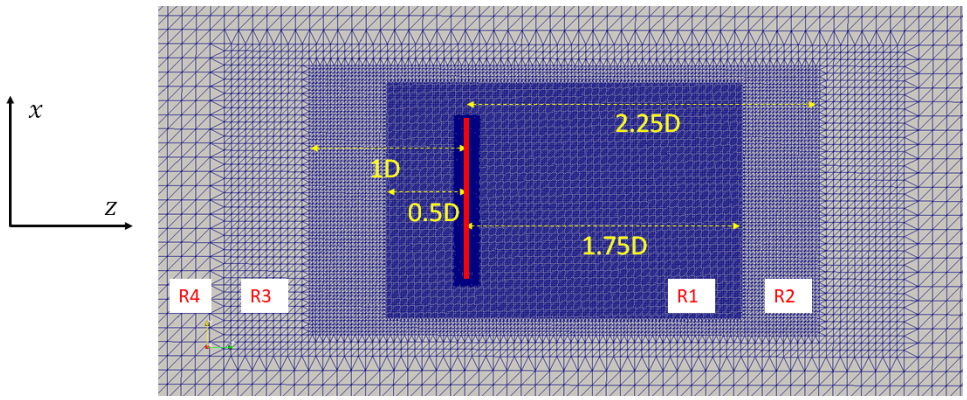

Fig. 5 Sectional view of the mesh used for the SR turbine simulation (red line denotes the location of the rotor)

zone R1 of $1.5D$ diameter is used up to $1.75D$ downstream with a mesh size of $c_r/4$. This is the mesh resolution used to analyze the near wake of the rotor. Additional cylindrical refinement zones R2 and R3 are used to transition the mesh from R1 to R4 and the mesh size increases by a factor of 2 in each of these transitions. Finally, a cylindrical refinement zone R0 is used in the immediate vicinity of the rotor with mesh size of $c_r/8$ to accurately capture the variation in distributed blade loads and the evolution of root and tip vortices.

The multi-rotor uses a similar grid, with a box refinement zone used for the propagation of turbulence and cylindrical refinement zones around each rotor. The c_r in the MR turbine is half of that in the SR turbine and thus, an additional refinement zone is used to transition from the mesh resolution used in the wake (i.e., $c_r/4$ with c_r corresponding to the root chord in the MR turbine) to that used at the turbulent inlet patch (i.e., $2c_r$ with c_r corresponding to the root chord in the SR turbine). The mesh for the SR turbine consists of about 20 million elements while the mesh for the MR turbine consists of about 125 million elements.

The following boundary conditions are used in the current simulations. At inlet, velocity components are prescribed including the turbulent inflow over an area as discussed in Section IV. A slip condition with no penetration is set at the top, bottom and side surfaces. This is possible since turbulent inflow is set only over a portion of the inlet. A natural pressure condition is set at the outlet. A second-order implicit time integration scheme [6] is employed with a step size corresponding to 2° rotation of the blade.

B. Comparison of V_z and TI contours

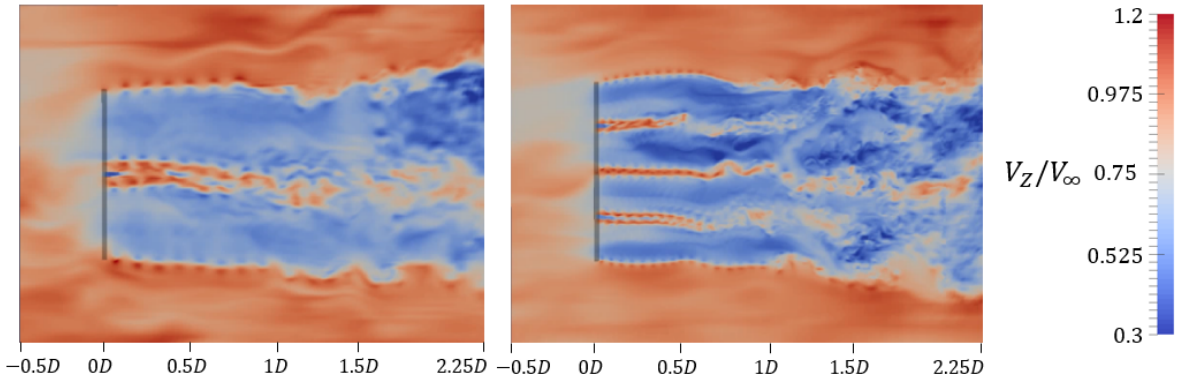

Fig. 6 Side view of instantaneous contours of V_z for the SR (left) and MR (right) turbines

Instantaneous contours of the axial velocity (V_z) normalized by V_∞ are shown in Figure 6 for the SR and MR turbines. The instantaneous contours clearly show the fluctuations in the ambient flow-field outside the wake of the rotors. Also,

the root and tip vortex roll-up is evident in the wake. Although it is difficult to estimate shear layer breakdown locations from instantaneous flow-fields, some evidence of breakdown can be seen in the wavy structures at the edge of the shear layer $1D$ downstream of the rotors. The instantaneous flow-fields also show the wake velocity deficit downstream of the rotors as well as the resulting expansion of the wake, although turbulent statistics are needed to further qualify these observations.

Subsequently, both the SR and MR simulation datasets are temporally averaged for 42 rotor revolutions corresponding to the SR (84 revolutions of MR) to give the contours presented in Figures 7, 8 and 9. The SR data is discussed first which is followed by the discussion and comparison of the MR data. The $\overline{V_z}$ contours for the SR clearly show the velocity deficit in the wake, with the deeper blue color in the outboard sections of the rotors which accounts for the majority of the lift generated and power produced by the rotor. The strong root vortices in the near-wake region diffuse into the surrounding slower flow-field as the wake evolves. Looking at the region in the immediate vicinity of the rotor along the centerline in Figure 7, a small deep blue region can be identified. This is due to the hub of the turbine, which is modeled by applying a drag force (based on hub's drag coefficient) in the corresponding elements in the mesh. The white arrow marks the onset of shear layer breakdown, which can be seen in the smearing of the sharp shear layer separating the wake from the surrounding free-stream. The slices taken at six downstream locations show the evolution of the $\overline{V_z}$ field in Figure 8. The sharply defined shear layer seen in the $0.5D$ slice becomes more diffuse in the further downstream locations and the root vortices are indistinguishable by $1.5D$. It is to be noted that there is no visual evidence of wake recovery as the axial velocity deficit seems to increase (deeper blue color) as we go downstream. The TI contours in Figure 9 clearly show the diffusion of the root vortices and the shear layer breakdown as we look downstream beyond $0.5D$. The axial TI contour in Figure 7 also show this phenomenon with the diffusion of the deeper red color at the outer edge of the rotor over the evolution of the wake.

Unlike the SR contours, the MR $\overline{V_z}$ contours in Figure 7 show some evidence of wake recovery beyond the $1.5D$ station characterized by a lighter blue color (see dashed box). Also, the TI contours in Figure 7 show higher wake turbulence up to the $1.5D$ station compared to the SR contours (see dashed box), potentially leading to faster mixing and wake recovery. It is interesting to note that the $\overline{V_z}$ contours for the MR shows an additional entrainment region between the adjacent rotors which is absent for the SR case. This high-speed air entrainment contributes to the mixing in the wake of the MR turbine, clearly evident along the centerline of Figure 7, particularly in the TI contour for MR.

C. Comparison of Wake Deficit and Added Turbulence

In order to quantitatively compare the axial velocity deficit in the wake as well as the turbulence intensity added to the ambient turbulent flow by the SR and MR turbines, we define the following quantities

$$\Delta\overline{V_z} = 1 - \overline{V_z} \tag{27}$$

$$\Delta TI = \begin{cases} -\sqrt{TI_{inlet}^2 - TI^2}, & \text{if } TI < TI_{inlet} \\ \sqrt{TI^2 - TI_{inlet}^2}, & \text{otherwise} \end{cases} \tag{28}$$

In Eq. 28, TI_{inlet} is the spatial average of the incoming turbulent intensity over a $2D \times 2D$ square centered at the turbine.

The non-dimensional $\Delta\overline{V_z}$ and ΔTI for the SR and MR turbines are shown in Figures 10 and 11, respectively. In the SR case, the dashed lines in both profiles show azimuthally averaged quantities. For the $\Delta\overline{V_z}$ profile, the two lines (i.e., solid and dashed lines) nearly overlap indicating that the current temporal averaging duration is sufficient. However, in the ΔTI profile some differences are seen between the two lines (i.e., solid and dashed lines) with a similar overall trend, which is expected since second-order statistics (such as TI) requires more data to attain statistical convergence. Note that azimuthal averaging is not applicable in the MR case. The $\Delta\overline{V_z}$ for the SR case shows an increasing velocity deficit profile over the distance considered in the plot. The higher velocity due to the root vortices diffuse and the $\Delta\overline{V_z}$ profile becomes more uniform over increasing downstream distance. The schematic on the right shows the section over which the quantities are plotted. The ΔTI profile for the SR also shows a generally increasing trend with the peaks corresponding to tip and root regions and they diffuse in the downstream direction. However, there is still significant non-uniformity in both the profiles at the $2.25D$ location.

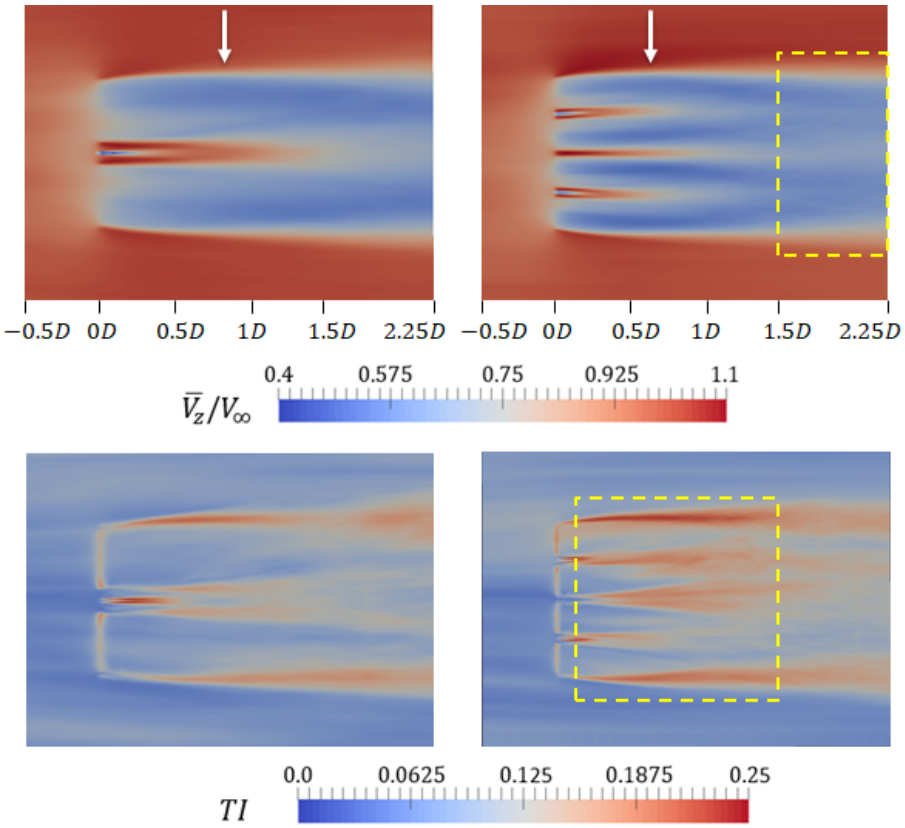

Fig. 7 Side view of time-averaged contours of $\overline{V_z}$ and TI for the SR (left) and MR (right) turbines

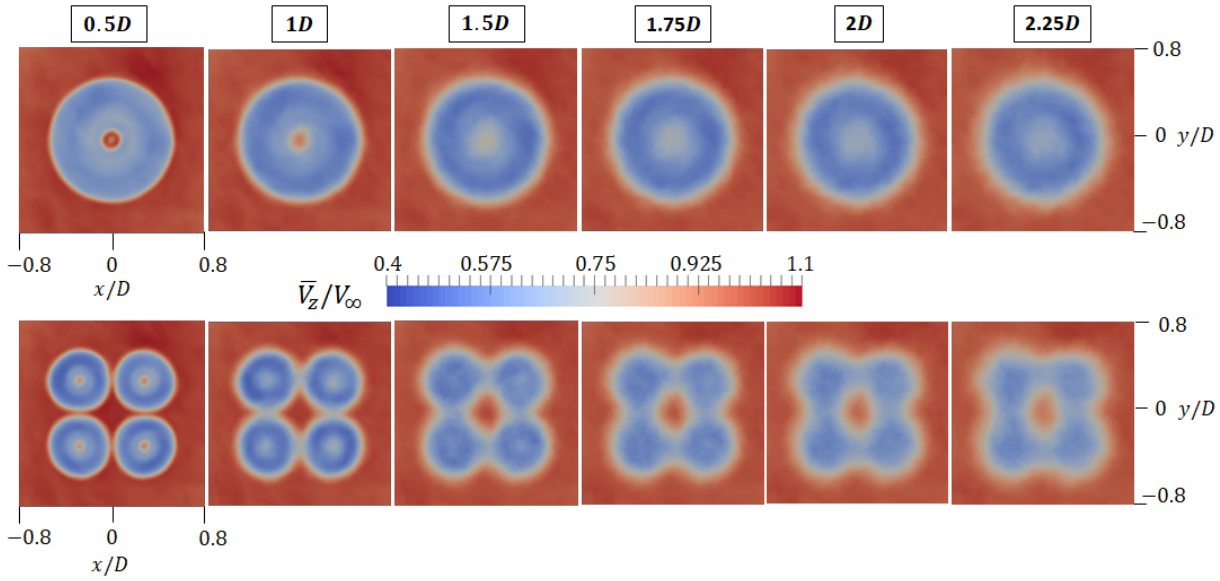

Fig. 8 Axial slices of time-averaged contours of $\overline{V_z}$ for the SR (top) and MR (bottom) turbines

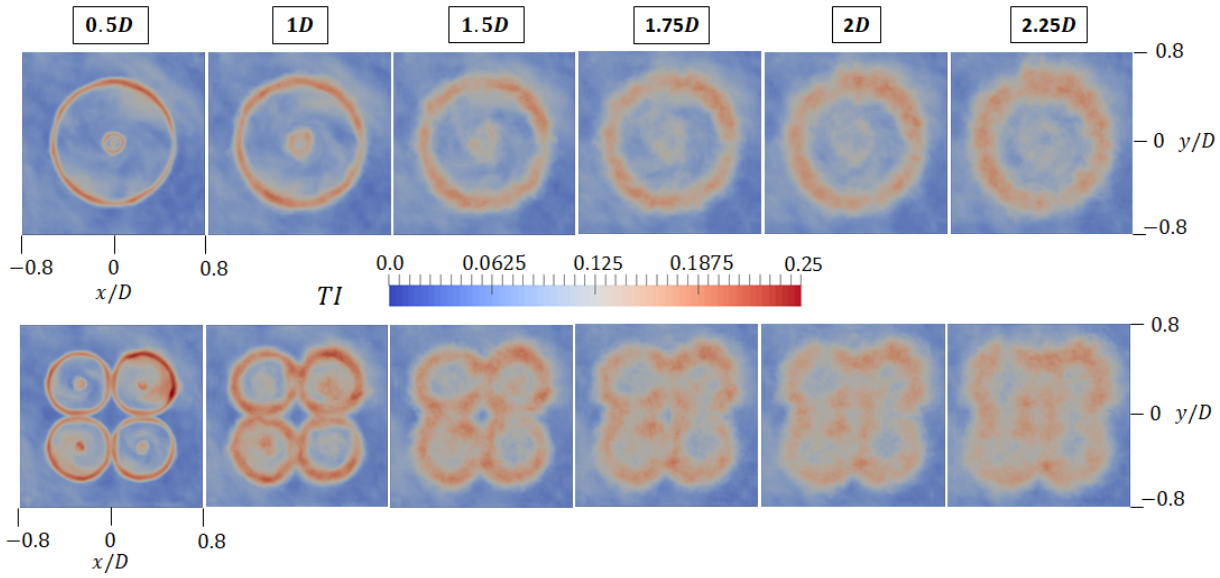

Fig. 9 Axial slices of contours of TI for the SR (top) and MR (bottom) turbines

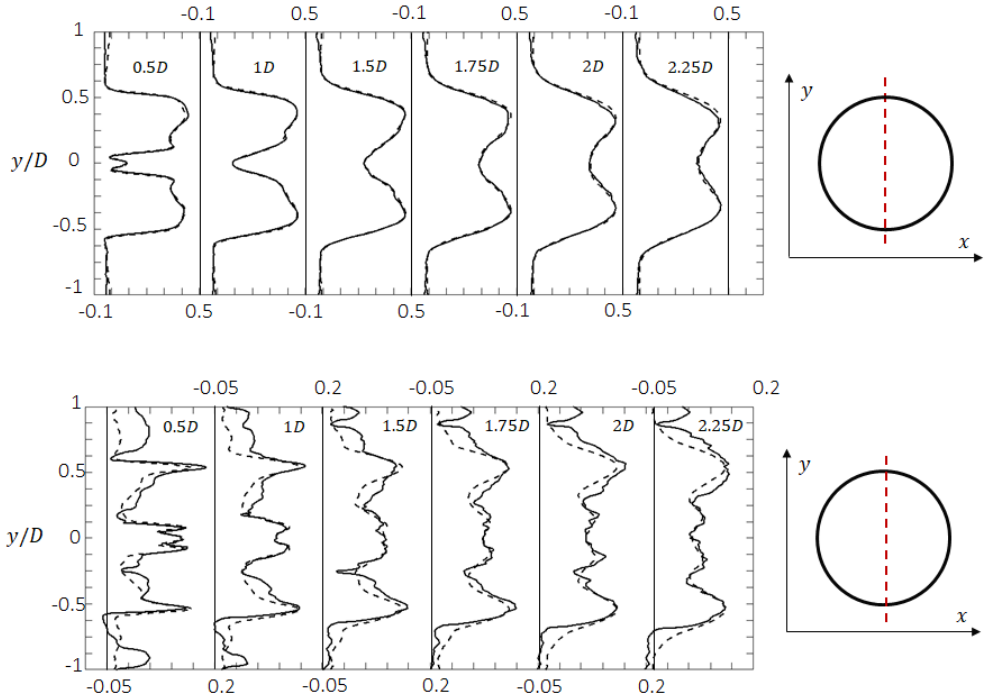

Fig. 10 Axial velocity deficit (top) and added TI (bottom) for the SR turbine

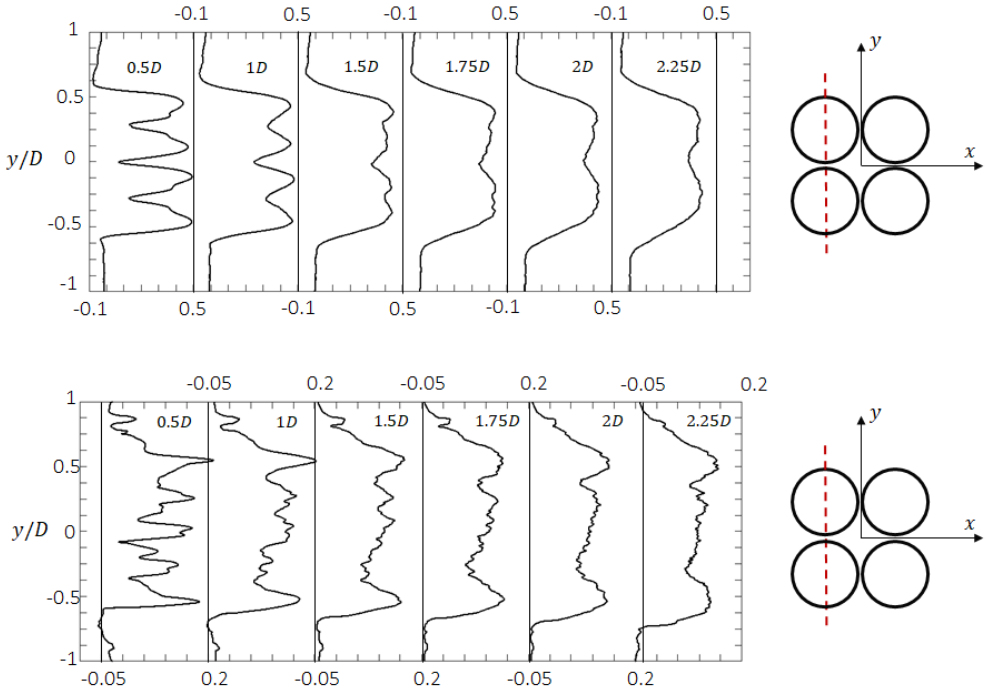

Fig. 11 Axial velocity deficit (top) and added *TI* (bottom) for the MR turbine

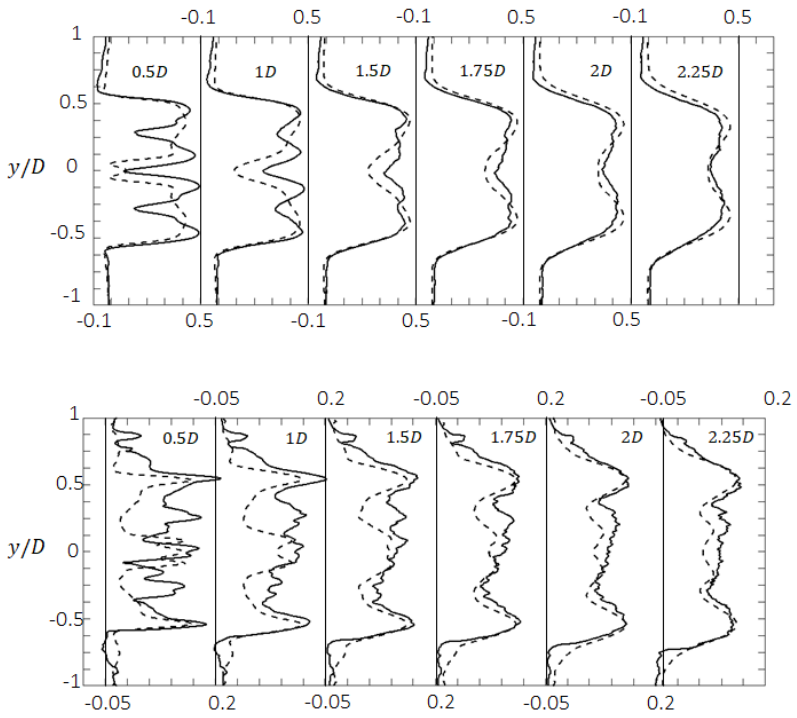

Fig. 12 Comparison of axial velocity deficit and added *TI* between SR (dashed) and MR (solid) turbines

On the other hand, the $\Delta\overline{V_z}$ for the MR case shows a small reduction from $1.5D$ to $2.25D$ downstream location, with the peaks corresponding to the tip region of individual rotors and as before, they diffuse in the downstream direction. This can also be seen in Figure 12 where the azimuthal averages for the SR are compared with the MR profiles and the MR shows lower $\Delta\overline{V_z}$ compared to the SR case. Compared to the SR profile, the MR profile shows higher non-uniformity at the near-rotor stations (up to $1D$) in both quantities due to the presence of multiple rotors which aids the mixing and recovery process. Also, the ΔTI profile for the MR turbine starts to decrease in magnitude at higher downstream distances (for example, comparing the $1D$ and $1.5D$ stations). The non-uniformity of the $\Delta\overline{V_z}$ has also reduced beyond $1D$ compared to the SR case, clearly indicating a faster wake recovery in the MR case.

VI. Conclusions and Future Work

A high-fidelity LES study comparing the wake deficit and turbulent intensity values between a multi-rotor configuration and an equivalent single rotor was performed. A computationally tractable ALM implementation was utilized for the rotors while resolved incoming turbulence without any shear was imposed upstream of the turbine to study its effect on shear layer breakdown and wake recovery. The MR configuration showed evidence of faster wake recovery as compared to the SR case. The higher degree of uniformity in the $\Delta\overline{V_z}$ as well as reduced peaks in the wake deficit for the MR turbine as compared to SR highlights the potential benefits of using such configurations in large wind farm scenarios (for example, high wake losses and inter-turbine spacing due to the use of large single rotors has been documented [22]).

In the future, we plan to further quantify the benefits of the multi-rotor turbine configuration under atmospheric boundary layer including both turbulence and shear. Further, several aspects of the wind turbine have been currently neglected in the computational modeling, including the tower, nacelle and booms that may exhibit significant aerodynamic effects on the wake deficit and added turbulence. Finally, highly resolved simulations such as the one in this study can be used to examine detailed aspects of wind turbine near wake dynamics such as tip vortex interactions between adjacent rotors in multi-rotor configurations, and their influence on shear layer breakdown and wake mixing as well as recovery.

Acknowledgment

This project is sponsored by the New York State Energy Research Development Authority (NYSERDA), with cost-sharing from the General Electric Co. (GE). The technical monitors are Richard Bourgeois (NYSERDA), Siddharth Ashar (GE) and Maxwell Peter (GE). The authors are grateful for the sponsorship and the technical input provided by the monitors. NYSERDA has not reviewed the information contained herein, and the opinions expressed in this report do not necessarily reflect those of NYSERDA or the State of New York. The authors also thank the Center for Computational Innovations (CCI) at Rensselaer Poytechnic Institute for providing computational resources essential to the completion of this work.

References

[1] Laan, M. P. v. d., Andersen, S. J., Ramos García, N., Angelou, N., Pirrung, G. R., Ott, S., Sjöholm, M., Sørensen, K. H., Vianna Neto Julio, X., Kelly, M., Mikkelsen, T., and Larsen, G. C., "Power curve and wake analyses of the Vestas multi-rotor demonstrator," *Wind Energy Science*, Vol. 4, No. 2, 2019, pp. 251–271.

[2] Chasapogiannis, P., Prospathopoulos, J. M., Voutsinas, S. G., and Chaviaropoulos, T. K., "Analysis of the aerodynamic performance of the multi-rotor concept," *Journal of Physics: Conference Series*, Vol. 524, IOP Publishing, 2014, p. 012084.

[3] Jamieson, P., Chaviaopoulos, T., Voutsinas, S., Branney, M., Sieros, G., and Chasopogiannis, P., "The structural design and preliminary aerodynamic evaluation of a multi-rotor system as a solution for offshore systems of 20MW or more unit capacity," *EWEC & Exhibition Barcelona, EWEA*, 2014.

[4] Ghaisas, N. S., Ghate, A. S., and Lele, S. K., "Large-eddy simulation study of multi-rotor wind turbines," *Journal of Physics: Conference Series*, Vol. 1037, IOP Publishing, 2018, p. 072021.

[5] Troldborg, N., Sørensen, J. N., and Mikkelsen, R., "Actuator line simulation of wake of wind turbine operating in turbulent inflow," *Journal of physics: conference series*, Vol. 75, IOP Publishing, 2007, p. 012063.

[6] Tran, S., and Sahni, O., "Finite element based large eddy simulation using a combination of the variational multiscale method and the dynamic Smagorinsky model," *Journal of Turbulence*, Vol. 18, 2017, pp. 391–417.

[7] Wang, Z., and Oberai, A. A., "A mixed large eddy simulation model based on the residual-based variational multiscale formulation," *Physics of Fluids*, Vol. 22, No. 7, 2010, p. 075107.

[8] Tran, S., Cummings, R., and Sahni, O., "Finite element based large eddy simulation of flow over bluff bodies," *Computer & Fluids*, Vol. 158, No. 24, 2017, pp. 221–235.

[9] Tran, S., and Sahni, O., "Large eddy simulation based on the residual-based bariational multiscale method and Lagrangian dynamic Smagorinsky model," *54th AIAA Aerospace Sciences Meeting*, 2016. AIAA Paper 2016-0341.

[10] Hughes, T. J., and Sangalli, G., "Variational multiscale analysis: the fine-scale Green's function, projection, optimization, localization, and stabilized methods," *SIAM Journal on Numerical Analysis*, Vol. 45, No. 2, 2007, pp. 539–557.

[11] Oberai, A., and Wanderer, J., "Variational formulation of the Germano identity for the Navier-Stokes equations," *Journal of Turbulence*, , No. 6, 2005, p. N7.

[12] Meneveau, C., Lund, T. S., and Cabot, W. H., "A Lagrangian dynamic subgrid-scale model of turbulence," *Journal of Fluid Mechanics*, Vol. 319, 1996, pp. 353–385.

[13] Manwell, J. F., McGowan, J. G., and Rogers, A. L., *Wind energy explained: theory, design and application*, John Wiley & Sons, 2010.

[14] Sørensen, J., and Shen, W., "Numerical modeling of wind turbine wakes," *Journal of fluids engineering*, Vol. 124, No. 2, 2002, pp. 393–399.

[15] Dykes, K. L., and Rinker, J., "WindPACT Reference Wind Turbines," Tech. rep., National Renewable Energy Lab.(NREL), Golden, CO (United States), 2018.

[16] Jonkman, J., Butterfield, S., Musial, W., and Scott, G., "Definition of a 5-MW reference wind turbine for offshore system development," Tech. rep., National Renewable Energy Lab.(NREL), Golden, CO (United States), 2009.

[17] Kirby, A. C., Hassanzadeh, A., Mavriplis, D. J., and Naughton, J. W., "Wind Turbine Wake Dynamics Analysis Using a High-Fidelity Simulation Framework with Blade-Resolved Turbine Models," *2018 Wind Energy Symposium*, 2018, p. 0256.

[18] Wu, Y.-T., and Porté-Agel, F., "Atmospheric turbulence effects on wind-turbine wakes: An LES study," *Energies*, Vol. 5, No. 12, 2012, pp. 5340–5362.

[19] Jonkman, B. J., "TurbSim user's guide: Version 1.50," Tech. rep., National Renewable Energy Lab.(NREL), Golden, CO (United States), 2009.

[20] Churchfield, M. J., Lee, S., Michalakes, J., and Moriarty, P. J., "A numerical study of the effects of atmospheric and wake turbulence on wind turbine dynamics," *Journal of turbulence*, , No. 13, 2012, p. N14.

[21] Elliott, D., Schwartz, M., and Scott, G., "Wind Shear and Turbulence Profiles at Elevated Heights: Great Lakes and Midwest Sites (Poster)," Tech. rep., National Renewable Energy Lab.(NREL), Golden, CO (United States), 2009.

[22] Nygaard, N. G., "Wakes in very large wind farms and the effect of neighbouring wind farms," *Journal of Physics: Conference Series*, Vol. 524, IOP Publishing, 2014, p. 012162.